Lattice Boltzmann framework for accurate NMR simulation in porous media

Ivan Rybin, Igor Shikhov, and Christoph H. Arns*
School of Minerals and Energy Resources Engineering, The University of New South Wales, Sydney, Australia

(Received 4 August 2020; revised 2 February 2021; accepted 20 April 2022; published 10 May 2022)

Nuclear magnetic resonance (NMR) responses of fluids saturating porous media arise from complex relaxation-diffusion dynamics of polarized spins. These constitute a sensitive probe of the microstructure and are described by the Bloch-Torrey equations. An NMR simulation framework based on an augmented lattice Boltzmann method aimed at the fine-scale resolution of nuclear polarization density is presented. The approach encapsulates the time evolution of the full magnetization vector and naturally incorporates the mechanisms of diffusional transport. Spin dephasing mechanisms are fully resolved at tomogram voxel scale to account for magnetic field inhomogeneity. The approach is validated against analytical solutions of spin-echo decays for simple pore geometries. An application to a nano-computed-tomography image of chalk with inhomogeneous internal fields yields T_2 spectral measures in good agreement with experiment and illustrates the spatial pore-scale dynamics of net magnetization. Findings establish the feasibility of the framework for pure diffusion and present an approach vector to modeling the evolution of magnetization under flow conditions.

DOI: 10.1103/PhysRevE.105.055304

I. INTRODUCTION

Morphological characterization of porous media is a contemporary challenge encountered in medicine [1], microbiology [2], physical chemistry [3], soil science [4], and petroleum engineering [5]. Though the sensitivity of an nuclear magnetic resonance (NMR) signal to its environment makes it a useful phenomenon for noninvasive characterization of porous systems, this response is nontrivial as complex relaxation-diffusion dynamics arise from spatial heterogeneity and local field anisotropy. Accurate computational solutions can provide a powerful testbed for model attributes and experimental parameters to aid in the interpretation of NMR measurements. While analytical solutions describing NMR relaxation in idealized systems do exist [6–9], samples that exhibit complexity necessitate a numerical treatment. Random-walk algorithms individually model the thermal motion of polarized. species; they were validated for simple geometries without internal field gradients [10] and extended to the case of a constant field gradient [11] and arbitrary inhomogeneous fields [12,13]. An alternative approach to random walks is based on finding the finite-difference solution to the Bloch-Torrey (BT) equation [14] to directly evaluate the evolution of macroscopic net magnetization of a system discretized in space and time [15]. This has found applications in magnetic resonance imaging (MRI) where the magnetization vector is simulated in each imaging voxel [16]. The coarse resolution of MRI facilitates the assumption of self-contained elementary volumes under isotropic diffusion constituting effective property spatial subsets of the sample that evolve independently. Naughton *et al.* [17] have applied the lattice Boltzmann method to integrate the BT equation in simulating diffusion MRI responses of tissue models. The work implements the approach in the context of diffusion MRI in a medium composed of cells with varying cell membrane permeability under a constant gradient of the MR device.

High-resolution (micro-) x-ray computed tomography (XCT) [18] as a complementary technique provides significantly higher resolution than MRI. NMR or MRI simulations on fully resolved complex structures may provide additional insight into fine-scale morphology, surface interactions, and fluid transport characteristics.

This work presents a fine-scale general purpose NMR simulation framework based on the abstractions of the lattice Boltzmann method (LBM) coupled with a modified treatment of the Bloch-Torrey equations. Due to the fundamental assumption of magnetization transportation, the approach inherently incorporates the exchange of magnetization carriers due to molecular self-diffusion. The principal mechanisms of magnetization evolution are accounted for locally using the Bloch-Torrey equations, with magnetization transport facilitated by the LBM formalism, also enabling the approach to encode spin dynamics in arbitrary inhomogeneous magnetic fields.

A. The Bloch-Torrey equation

The realignment of the net spatial average nonequilibrium magnetization $\boldsymbol{m}$ of a macroscopic set of resonant atomic nuclei with a local magnetic field $\boldsymbol{B}$ after an RF pulse at a site $\boldsymbol{r}$ belonging to a fluid-bearing domain Ω is described by the Bloch-Torrey equation [14]:

$$\frac{\partial \boldsymbol{m}}{\partial t}(\boldsymbol{r}) = \underbrace{\nabla \cdot \boldsymbol{D}\nabla \boldsymbol{m}}_{(1)} - \underbrace{\begin{bmatrix} m_x/T_{2b} \\ m_y/T_{2b} \\ (m_z - m_0)/T_{1b} \end{bmatrix}}_{(2)} + \underbrace{\gamma(\boldsymbol{m} \times \boldsymbol{B})}_{(3)}, \quad (1)$$

*c.arns@unsw.edu.au

where $\boldsymbol{m} = [m_x,\ m_y,\ m_z]$ and m_0 is the magnitude of magnetization at equilibrium ($t = 0$).

The principal evolution terms are (1) magnetization self-diffusion with tensor $\boldsymbol{D}$, (2) bulk relaxation with time constants T_{1b} and T_{2b}, and (3) precessional phase offset in the rotating frame of reference, where γ is the gyromagnetic ratio of the nuclear species. The continuum BT equation is accompanied by the boundary condition:

$$\begin{aligned} &\hat{\boldsymbol{n}}_A \cdot \boldsymbol{D}_A \nabla \boldsymbol{m}_A - \boldsymbol{m}(\boldsymbol{r})\rho_{\alpha,A} \\ &= -\hat{\boldsymbol{n}}_B \cdot \boldsymbol{D}_B \nabla \boldsymbol{m}_B - \boldsymbol{m}(\boldsymbol{r})\rho_{\alpha,B} = \quad \Leftrightarrow \boldsymbol{r} \in d\Omega, \\ &k_{AB}(\boldsymbol{m}_A - \boldsymbol{m}_B) \end{aligned} \tag{2}$$

where $\hat{\boldsymbol{n}}$ denotes the unit normal to the fluid domain boundary $d\Omega$ at $\boldsymbol{r}$, $\rho_{\alpha,X}$ denotes the surface relaxivity constant for a given domain X, α denotes either a T_2 or T_1 process, and k_{AB} denotes the exchange coefficient between domains A and B.

The localized field behavior at the fluid-solid interface is a special case of Eq. (2) whereby we assume null magnetization throughout the solid domain, $\boldsymbol{m}_B = \boldsymbol{0}$, and an impermeable boundary by setting $k = 0$. The solid-fluid discontinuity is mathematically seen as the boundary condition

$$\hat{\boldsymbol{n}} \cdot \boldsymbol{D} \nabla \boldsymbol{m} - \boldsymbol{m}(\boldsymbol{r})\rho_\alpha = \boldsymbol{0} \quad \Leftrightarrow \boldsymbol{r} \in d\Omega. \tag{3}$$

Computational treatment of the boundary in classical finite-difference schemes is a challenge; evaluating magnetization at fluid nodes adjacent to the solid phase presents a mathematical discontinuity, as the magnetization throughout the latter is assumed to be zero. To ensure spatially continuous magnetization for differential operations, the typical approach sets a fictitious magnetization value at the boundary node consistent with the chosen boundary condition, in this case Eq. (3). Its value is a function of the magnetization at the fluid node adjacent to the discontinuity. This is achieved by a differential treatment of Eq. (3). Consider a site A in the fluid phase with magnetization $\boldsymbol{m}_A$ located adjacent to a solid site (B), whose fictitious magnetization $\boldsymbol{m}_B$ represents the unknown boundary value. Further, assume isotropic diffusion at A. Discretize Eq. (3) on a Cartesian grid of side length δx. Note that the transverse and longitudinal magnetization components' relaxation is numerically distinct, as the former diminishes in time (exponential decay), while the latter increases (negative exponential in the limit of M_0 for inversion recovery). The latter necessitates the distinction between surface relaxivities for T_2 and T_1 mechanisms. To that end, ρ_α, where $\alpha = 2$ or 1 will denote the surface relaxivity constants for T_2 or T_1 processes, respectively. Assume spatially isotropic diffusion with scalar coefficient D_0. Rearrange Eq. (3) to obtain

$$\begin{aligned} &m_{B,xy} = \lambda_2 m_{A,xy} \ \text{ and } \ m_{B,z} = \lambda_1 m_{A,z} + \zeta_1, \ \text{ where} \\ &\lambda_\alpha = \frac{2D_0 - \rho_\alpha \delta x}{2D_0 + \rho_\alpha \delta x} \ \text{ and } \ \zeta_\alpha = \frac{2\rho_\alpha \delta x}{2D_0 + \rho_\alpha \delta x}. \end{aligned} \tag{4}$$

The above coefficients constitute an effective method of mathematically formulating the solid-fluid interface as a differential boundary condition to incorporate surface relaxation modes in finite-difference schemes, and will be used in a similar manner in the proposed approach [15].

II. THE NMR-LBM STRATEGY

The proposed approach draws from the abstract fluid dynamics of the lattice Boltzmann method to define a magnetization evolution algorithm in Cartesian discretized Euclidean space in discrete time. Herein we will limit ourselves to the case of self-diffusion of magnetized particle groups on the macroscopic scale as described by the three terms of magnetization transport (1), bulk relaxation (2), and spin dephasing (3) in the Bloch-Torrey equation [Eq. (1)].

A. Magnetization transport

The LBM is a numerical framework of modeling fluid dynamics [19]. As opposed to traditional computational approaches to modeling time-evolving systems, LBM does not directly resolve the governing equation (in the case of fluid dynamics, the Navier-Stokes equation) at the microscopic scale. Instead, it abstracts the fundamental dynamic units to particle assemblages (quanta) undergoing probabilistic motion on a geometric lattice in discrete time while interacting with each other as well as the boundary. This mesoscopic scale formalism leads back to the total physical quantity at any given lattice location as the sum over these quanta. The well-known LBM equation is stated as follows [20]:

$$f_i(\boldsymbol{r} + \boldsymbol{e}_i, t + \delta t) = f_i(\boldsymbol{r}, t) + \mathcal{K}, \tag{5}$$

$$\mathcal{K} = \frac{1}{\tau}\left[f_i^{\text{eq}}(\boldsymbol{r}, t) - f_i(\boldsymbol{r}, t)\right], \tag{6}$$

where f_i is the flux probability density function along basis element $\boldsymbol{e}_i$, τ is the local relaxation time parameter, $\mathcal{K}$ is the Bhatnagar-Gross-Krook (BGK) collision operator, and f_i^{eq} is the equilibrium distribution function. Recalling the assumption of pure diffusion, the latter becomes

$$f_i^{\text{eq}}(\boldsymbol{r}, t) = w_i \rho(\boldsymbol{r}, t) \ \Leftrightarrow \ \rho(\boldsymbol{r}, t) = \sum_i f_i(\boldsymbol{r}, t), \tag{7}$$

where $\rho(\boldsymbol{r}, t)$ is the fluid density at $\boldsymbol{r}$ and time t and w_i is the directional weight determined by the discretization of the continuous flux probability density along the lattice basis.

NMR-LBM draws on Eq. (6) and (7) to resolve the mechanics of diffusional magnetization exchange as per the Bloch-Torrey equation. To that end, we assert a conceptual equivalence between the local fluid concentration probability function $f_i(\boldsymbol{r}, t)$ and a magnetization probability density vector function $\boldsymbol{q}_i(\boldsymbol{r}, t)$ with components $q_{i,x}$, $q_{i,y}$, and $q_{i,z}$. The magnetization components carried by a virtual fluid stream move along a given lattice direction at a given site $\boldsymbol{r}$, such that the local magnetization density $\boldsymbol{m}(\boldsymbol{r})$ is obtained by a sum over $\boldsymbol{q}_i(\boldsymbol{r})$:

$$\boldsymbol{m}(\boldsymbol{r}, t) = [m_x, \quad m_y, \quad m_z]^T = \sum_{i=0}^{Q-1} \boldsymbol{q}_i(\boldsymbol{r}, t), \tag{8}$$

where i denotes lattice direction; $i \in \{1, \ldots, Q-1\}$ for each of $Q-1$ neighboring cells and $i = 0$ for the resting particle.

The time evolution of magnetization lattice components is computed in a multistep algorithm. After collision and streaming (1), magnetization streams are subjected to a series of finite-difference operations as per the BT equations

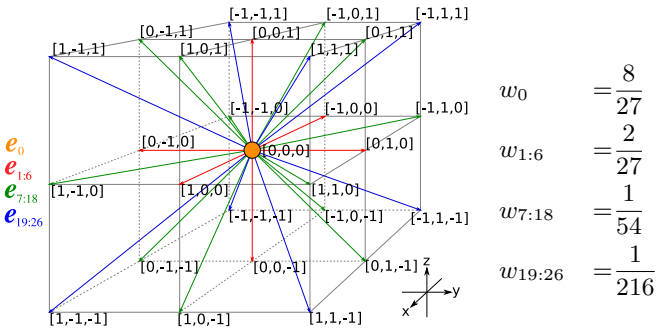

FIG. 1. D3Q27 basis $\{\boldsymbol{e}_{0:26}\}$ illustrated in 3D perspective projection with respective weights $\{w_{0:26}\}$: twenty-six neighbors in addition to the rest particle.

to incorporate (2) bulk relaxation and (3) spin dephasing effects. To obtain the core NMR-LBM dynamics equation, rearrange Eq. (6), substituting q for f, for an explicit expression of local directional magnetization density's time evolution:

$$\boldsymbol{q}_{i,(1)} = \boldsymbol{q}_i(\boldsymbol{r}, t+\delta t) = \boldsymbol{q}_i(\boldsymbol{r}-\boldsymbol{e}_i, t) + \boldsymbol{\Xi}(\boldsymbol{r}-\boldsymbol{e}_i, t), \tag{9}$$

where $\boldsymbol{q}_{i,(1)}$ denotes a magnetization stream along $\boldsymbol{e}_i$ after the collision-streaming step, $\boldsymbol{\Xi}$ denotes the magnetization collision function, analogously to $\mathcal{K}$ in Eq. (6) and δt denotes the elementary simulation time step. For purely diffusional systems, the relaxation time parameter τ will be set to 1 in all simulations in this work; the time step is obtained as $\delta t = \delta x^2/(6D_0)$, where δx is the side length of the finite-volume element in the Cartesian computational domain. Herein, unless explicitly stated otherwise, these finite volumes will be referred to as "voxels," to the extent that denotes the three-dimensional (3D) generalization of the pixel. The choice of nomenclature becomes readily apparent at a later point, when computations are performed on tomographic images. This implementation utilizes lattice discretization models similarly to the CFD LBM method [21]. In this investigation, the 3D, 27-velocity-component (D3Q27) model (Fig. 1) will be used, as the findings of Ref. [22] suggest a positive correlation between velocity set size and accuracy in the context of NMR responses of simple 2D systems.

B. Bulk relaxation

Bulk relaxation mechanisms affect magnetization across the entire domain in accordance with the time constants, T_{2b} for transverse, and T_{1b} for longitudinal magnetization. These are introduced into the NMR-LBM formalism [Eq. (9)] with the magnetization stream $\boldsymbol{q}_{i,(1)}$ undergoing bulk relaxation in accordance with the Euler finite-difference approximation of the second term of Eq. (1):

$$\boldsymbol{q}_{i,(2)} = \boldsymbol{q}_{i,(1)} - \left[\frac{q_{i,x,(1)}}{T_{2b}}, \quad \frac{q_{i,y,(1)}}{T_{2b}}, \quad \frac{q_{i,z,(1)} - w_i m_0}{T_{1b}}\right]^T \delta t, \tag{10}$$

where $q_{i,x,(1)}$, $q_{i,y,(1)}$, and $q_{i,z,(1)}$ respectively denote the x, y, and z, magnetization components of a stream along $\boldsymbol{e}_i$ and δt denotes the simulation time step. Note the inclusion of the factor w_i in Eq. (10), signifying that each directional magnetization component contributes to the local longitudinal repolarization in accordance with its lattice weight.

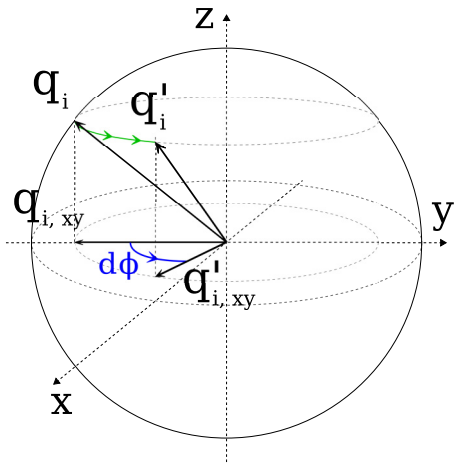

FIG. 2. Diagram of finite-difference phase increment operation on a local magnetization vector q_i in $\mathbb{R}^3$.

C. Phase encoding

Consider a simulation node at $(\boldsymbol{r}, t=0)$ with a net nonequilibrium magnetization $\boldsymbol{m}$ in a region where the local magnetic field $\boldsymbol{B}$ deviates from the externally applied magnetic field $\boldsymbol{B_0} = [0, 0, B_0]$. In the rotating frame of reference, this magnetization will sustain a transverse phase offset as per the Bloch-Torrey formulation [Eq. (1)]

$$\left.\frac{\partial \boldsymbol{m}}{\partial t}\right|_{\phi} = \gamma(\boldsymbol{m} \times \boldsymbol{B}), \tag{11}$$

where the subscript ϕ denotes magnetization evolution due to local dephasing.

Taking the Euler approximation of Eq. (11) over δt assuming fine time discretization and a uniformly z-directed $\boldsymbol{B_0}$, the phase evolution of $\boldsymbol{m}$ may be expressed as a vector rotation R_z about the z axis with argument $d\phi$ [Eq. (12)] [23]. The resulting procedure [Eq. (13)] induces a phase offset in magnetization streams at each time step to encode spin dephasing commensurate with local field deviations from $\boldsymbol{B_0}$, illustrated in Fig. 2 (the relative amount of phase accumulation $d\phi$ is highly exaggerated),

$$d\phi = \gamma \|\boldsymbol{B} - \boldsymbol{B_0}\| \delta t, \tag{12}$$

$$\boldsymbol{q}_{i,(3)} = R_z(d\phi)\boldsymbol{q}_{i,(2)}, \tag{13}$$

$$R_z(\alpha) = \begin{bmatrix} \cos(\alpha) & -\sin(\alpha) & 0 \\ \sin(\alpha) & \cos(\alpha) & 0 \\ 0 & 0 & 1 \end{bmatrix}, \tag{14}$$

D. Operator splitting

The bulk relaxation and dephasing differential operations on the magnetization vector are applied symmetrically around the collision-streaming operation $\boldsymbol{\Xi}$. Consider an additive magnetization evolution operator $\mathcal{M}$ acting for a duration δt on the magnetization vector carried by stream $\boldsymbol{q}_i$; in a given time step, this operator is applied for duration $\delta t/2$ before density is computed locally and resulting streams are obtained and again applied for a duration $\delta t/2$ to each of the latter.

Algorithm 1: NMR-LBM core

Require: $\boldsymbol{q}_i(\boldsymbol{r}-\boldsymbol{e}_i,t),\ \forall\, i$
Obtain: $\boldsymbol{q}_i(\boldsymbol{r},t+\delta t)\ \forall\, i$
$\boldsymbol{m}' \leftarrow \boldsymbol{0}$
for $i \leftarrow \{i \in \mathbb{Z} \mid 0 \le i < \mathrm{Q}\}$ **do**
  $\boldsymbol{q}_{i,(0)} \leftarrow \boldsymbol{q}_i(\boldsymbol{r}-\boldsymbol{e}_i,t)$ — incoming stream
  $\boldsymbol{q}_{i,(\mathcal{M})} \leftarrow \mathcal{M}(\frac{\delta t}{2})\left[\boldsymbol{q}_{i,(0)}\right]$ — magnetization 1
  $\boldsymbol{m}' \leftarrow \boldsymbol{m}' + \boldsymbol{q}_{i,(\mathcal{M})}$
end
for $i \leftarrow \{i \in \mathbb{Z} \mid 0 \le i < \mathrm{Q}\}$ **do**
  $\boldsymbol{q}_i^{eq} \leftarrow w_i \boldsymbol{m}'$ — equilibrium
  $\boldsymbol{\Xi}(\boldsymbol{r},t) \leftarrow \frac{1}{\tau}\left[\boldsymbol{q}_i^{eq} - \boldsymbol{q}_{i,(\mathcal{M})}\right]$ — collision
  $\boldsymbol{q}_{i,(\mathcal{M}\Xi)} \leftarrow \boldsymbol{q}_{i,(\mathcal{M})} + \boldsymbol{\Xi}(\boldsymbol{r},t)$ — streaming
  $\boldsymbol{q}_{i,(\mathcal{M}\Xi\mathcal{M})} \leftarrow \mathcal{M}(\frac{\delta t}{2})\left[\boldsymbol{q}_{i,(\mathcal{M}\Xi)}\right]$ — magnetization 2
  $\boldsymbol{q}_i(\boldsymbol{r},t+\delta t) \leftarrow \boldsymbol{q}_{i,(\mathcal{M}\Xi\mathcal{M})}$
end

The compound magnetization evolution operator can be formulated as follows:

$$\mathcal{M}(\delta t)[\boldsymbol{q}_i] = \{\boldsymbol{C_w} - (\boldsymbol{C_w} - \boldsymbol{q}_i)\exp[\boldsymbol{C_R}(\delta t)]\}R_z[d\phi(\delta t)], \quad (15)$$

where $\mathcal{M}(\delta t)$ acts on a stream $\boldsymbol{q}_i$ for a duration δt, with constants

$$\boldsymbol{C_R}(\delta t) = \left[\tfrac{-\delta t}{T_{2,b}} \quad \tfrac{-\delta t}{T_{2,b}} \quad \tfrac{-\delta t}{T_{1,b}}\right], \quad (16)$$

$$\boldsymbol{C_w} = [0 \quad 0 \quad w_i], \quad (17)$$

and phase increment $d\phi$ evaluated as per Eq. (12).

In this algorithm, the state of evolution of $\boldsymbol{q}_i$ within a time step is documented using sequential subscript notation, with

(1) $\boldsymbol{q}_{i,(\mathcal{M})}$ denoting the application of half of our magnetization time-evolution operator $\mathcal{M}$,

(2) $\boldsymbol{q}_{i,(\mathcal{M}\Xi)}$ denoting the result of the streaming operation on a local density and

(3) $\boldsymbol{q}_{i,(\mathcal{M}\Xi\mathcal{M})}$ signifying the second half of the magnetization time evolution.

This NMR-LBM strategy is outlined in Algorithm 1.

E. Boundary treatment

The boundary condition to the Bloch-Torrey equation, with its physical consideration of surface relaxation, is incorporated using a combination of the LBM bounce-back principle found in CFD literature and the BT boundary condition. Over a given time step, the boundary-bound magnetization stream is reflected along its antidirectional counterpart, having undergone a relaxation as per BT boundary condition [Fig. 3 and Eq. (18)], where λ_α and ζ_α denote the boundary constants in relaxing condition [Eq. (4)]. The fictitious $\boldsymbol{q}_2^*$ in Eq. (20) is seen as a stream entering the fluid phase from without to emulate bounce-back and relaxation on $\boldsymbol{q}_2$. Note the scaling of additive constant ζ_1 by the lattice weight along $\boldsymbol{e}_2$ in Eq. (18) for $\boldsymbol{q}_{2,z}^*$. The equilibrium function for the boundary is evaluated in a similar manner—Eq. (18) (with the exception of ζ_1 weighting) is applied to the magnetization density $\boldsymbol{m}$ in the fluid voxel adjacent to the boundary to evaluate the fictitious magnetization state across the boundary $\boldsymbol{m}^*$. Following, this fictitious state is used to evaluate the likewise fictitious collision function $\boldsymbol{\Xi}^*$ [Eq. (19)] to compute $\boldsymbol{q}_{1,(0)}$ at $(t+\delta t)$ [Eq. (20)].

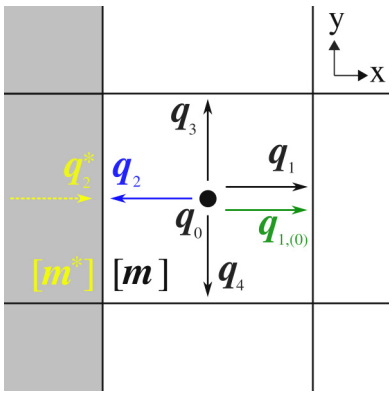

$$q_{2,x}^* = \lambda_2 q_{2,x}$$
$$q_{2,y}^* = \lambda_2 q_{2,y} \quad (18)$$
$$q_{2,z}^* = \lambda_1 q_{2,z} + \zeta_1 w_2$$

$$\boldsymbol{\Xi}^* = \frac{1}{\tau}\left[w_2 \boldsymbol{m}^* - \boldsymbol{q}_2^*\right] \quad (19)$$

$$\boldsymbol{q}_{1,(0)} = \boldsymbol{q}_2^* + \boldsymbol{\Xi}^* \quad (20)$$

FIG. 3. Illustration of NMR-LBM surface relaxation bounce-back principle with a D2Q5 lattice example (boundary voxels are depicted in gray; fluid voxels are in white).

F. Signal acquisition

The magnetization signal—S_{xy} for transverse and S_z for longitudinal—is acquired by taking the sum of local densities over all elements of the functional space, weighted by the local fluid concentration, equivalent to porosity $\phi(\boldsymbol{r})$. This operation captures the net nonequilibrium magnetization over the fluid domain Ω at time t:

$$S_{xy}(t) = \sum_{\boldsymbol{r}\in\Omega} \phi(\boldsymbol{r})[m_x(\boldsymbol{r},t)^2 + m_y(\boldsymbol{r},t)^2]^{\frac{1}{2}},$$
$$S_z(t) = \sum_{\boldsymbol{r}\in\Omega} \phi(\boldsymbol{r})[m_z(\boldsymbol{r},t)], \quad (21)$$

where m_x, m_y, and m_z are computed as per Eq. (8).

G. Pulse sequence simulation

The algorithm described above facilitates sequential evaluation of the system's localized magnetization states at finite time intervals defined by δt. Following, a combination of this computational solution with a simulated NMR pulse-acquisition sequence is introduced to model experimental encoding conditions. The Carr-Purcell-Meiboom-Gill pulse sequence (CPMG) [23,24] is a fundamental NMR experimental technique used to encode and acquire transverse magnetization decay, while partially compensating for secular T_2 relaxation effects due to dephasing. This is accomplished

by applying π (180°) refocusing RF field pulses at uniform time intervals t_E, while spin echoes occur at midpoints in time between refocusing pulses. Starting at time $t_0 = 0$ from a system at equilibrium with the external field $\boldsymbol{B}_0$,

$$\boldsymbol{m}(\boldsymbol{r}, t_0) = [0, 0, m_0]^T, \ \boldsymbol{q}_i(\boldsymbol{r}, t_0) = w_i \boldsymbol{m} \ \ \forall \boldsymbol{r} \in \Omega, \tag{22}$$

the $\pi/2$ pulse rotates $\boldsymbol{q}_i(\boldsymbol{r})$ for all $i \in \{0, 1, \ldots, Q-1\}$ and for all $\boldsymbol{r} \in \Omega$ by $\pi/2$ radians, placing the magnetization vector into the transverse plane. The field state then evolves as per Algorithm 1 for $n = 1, \ldots, N$, with simulated π pulses occurring between field evolution steps at $n = (2k-1)\nu_E$ and T_2 echo acquisitions [Eq. (21)] at $n = 2k\nu_E$, where $k \in \mathbb{Z}^+$ is an integer counter variable and $\nu_E = \lfloor t_E/(2\delta t) \rfloor$ is the integer approximation of the pulse-echo interval in terms of the discrete time unit δt.

The RF pulses are seen as instantaneous vector operations occurring between discrete time steps, also referred to as the "hard pulse approximation." This can be trivially modified by substituting the algebraic vector rotations with a series of finite-difference rotations in a similar manner to Eq. (12)–(14) by making $\boldsymbol{B_1}$ the torquing field. This modification would increase computational cost, arising from the refined timescale to avoid numerical stiffness. For all simulations performed herein, the hard pulse approximation is used.

III. ANALYTICAL VALIDATION

The decay of spin-echo amplitudes in porous media is governed by structural length $l_S = V/S$ (with V denoting volume and S denoting surface area), dephasing length $l_g = [D_0/(\gamma G)]^{1/3}$ (with G being the field gradient strength), and diffusional length $l_D = \sqrt{D_0 t}$. At short times in the free diffusion regime, where l_D is the shortest length and using the CPMG pulse sequence, the spin-echo decay is given by

$$M_{xy}(t, G) = M_0 \exp[-\gamma^2 G^2 D_0 (2t)^3/12]. \tag{23}$$

At longer diffusion times, in the motional averaging regime with $l_S \ll l_D, l_g$, one has [6,7,9]

$$M_{xy} = M_0 \exp\big[-c_1 r_{sg}^4 r_{dg}^2 \big(1 - c_2 r_{sg}^2 r_{dg}^{-2}\big)\big], \tag{24}$$

where $r_{sg} = l_S/l_g$, $r_{dg} = l_D/l_g$, and c_1 and c_2 are geometrical constants with $c_1 = 108/175$, $c_2 = 747/20$ for spheres, $c_1 = 7/36$, $c_2 = 297/14$ for circles, and $c_1 = 1/720$, $c_2 = 51/28$ for parallel plates. Comparisons between analytical solutions [Eq. (24)] and NMR-LBM simulations under restricted diffusion conditions for spherical, circular, and planar confining geometries over a set of field gradients are presented in Fig. 4. The results are for a characteristic diameter of $d = 2$ μm approximated on a square Cartesian mesh of side length $\epsilon = 66.667$ nm and the laboratory diffusion coefficient of water $D_0 = 2.15 \times 10^{-9}$ m^2/s, resulting in simulation time step $\delta t = 3.445 \times 10^{-7}$ s.

IV. RANDOM-WALK COMPARISON

The method is scrutinized by comparison to the well-known random-walk (RW) NMR simulation method. The latter fundamentally incorporates a Markov process to model the spatial dynamics of diffusing spin isochromats, or "walkers," as a discrete time sequence of steps of equal distance

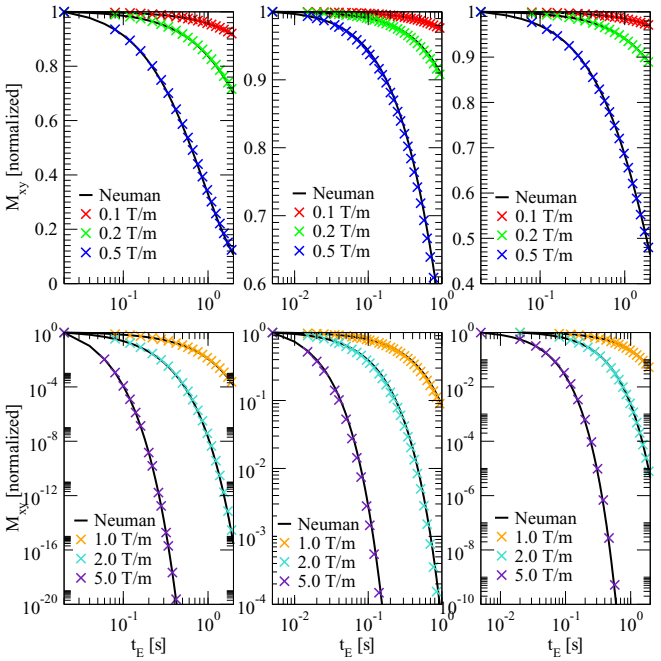

FIG. 4. Analytical solutions alongside simulated spin-echo intensity decays under restricted diffusion conditions for [(a) and (d)] planar, [(b) and (e)] circular, and [(c) and (f)] spherical geometries (1-, 2-, and 3-spheres, respectively).

in a randomly determined direction and independent of past system states. NMR mechanisms such as bulk and surface relaxation, as well as the influence of external field pulses is simulated by implementing storage of corresponding observable quantities at each walker, e.g., longitudinal and transverse polarization, spin phase, and a timescale. Statistical significance is attained by undertaking an appropriately large number of simulated walks. In this investigation, the random-walk simulations utilized 1 474 560 walkers.

The RW magnetization decay data are compared to NMR-LBM results for synthetic spherical pores of diameter 5 μm, approximated on square Cartesian grids of varying elementary resolution ϵ: $\epsilon = 250$ nm, $\epsilon = 125$ nm, $\epsilon = 83.3$ nm, and $\epsilon = 62.5$ nm, corresponding to discrete diameter of 20, 40, 60, and 80 voxels, respectively (Fig. 5). The internal magnetic field and the external field gradient were set to zero. Transverse surface relaxivity was set as $\rho_2 = 8.0$ μm/s, and bulk transverse relaxation time $T_{2,B} = 2.4$ s. The results (Fig. 5) demonstrate a trend of divergence of the decay magnitude between the two solvers as function of discretization level, converging to a constant factor in the limit of fine grid resolution. For reference the analytical fast diffusion limit (FDL) approximation for spheres,

$$M_T^{\mathrm{FDL}}(t) = \exp\left[-\frac{t}{T_{2,B}} - \frac{t}{T_{2,\mathrm{FDL}}}\right], \tag{25}$$

$$T_{2,\mathrm{FDL}} = (A\rho_2)^{-1}\frac{V}{S} = \frac{1}{6}\frac{d}{A\rho_2}, \tag{26}$$

is given as black lines for $A = 1.0$ and $A = 1.5$.

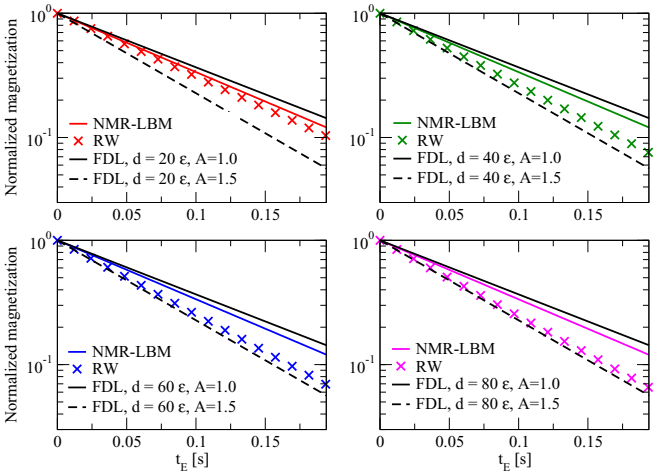

FIG. 5. Comparison of NMR-LBM and RW decay data alongside fast diffusion limit (FDL) analytical models for spherical pores 5 μm in diameter for various Cartesian discretizations: (a) $d = 20\ \epsilon$, $\epsilon = 250$ nm; (b) $d = 40\ \epsilon$, $\epsilon = 125$ nm; (c) $d = 60\ \epsilon$, $\epsilon = 83.3$ nm; and (d) $d = 80\ \epsilon$, $\epsilon = 62.5$ nm.

V. SIMULATION AND EXPERIMENT

Simulations were performed on a nano-XCT image (ZEISS Xradia 810 Ultra) of a chalk sample, recorded with cubic voxel size of side length $\epsilon = 64$ nm. The acquired tomogram was segmented into void space and solid using an active converging contour method [25,26]. A central 380^3 segmented region (Fig. 6) of the original 1000^3 tomogram was utilized in the following simulations; resultant porosity of 29.4% was close to experimentally obtained brine-saturated porosity of 30.2%. The diffusion coefficient of water was used $D_0 = 2.15 \times 10^{-9}$ m^2/s, yielding a simulation time step of $\delta t = 3.175 \times 10^{-7}$ s for chalk.

The choice of model parameters $\{\rho_2, D_0, T_{2b}, \chi_v\}$ was dictated by their experimentally measured values, with the exception of ρ_2. The latter was determined by matching an experimental T_2 spectrum with mercury intrusion capillary

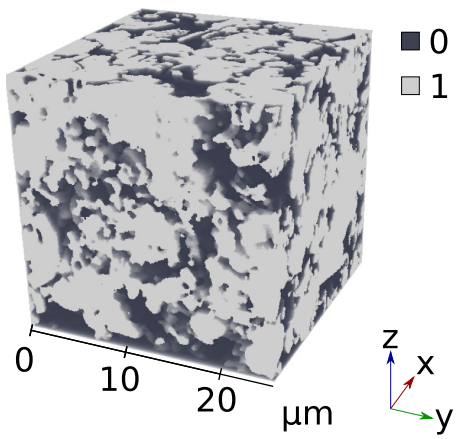

FIG. 6. Three-dimensional image of the chalk subsample digital segmentation used for simulations: cubic voxels of side length $\epsilon = 64$ nm, "0" labels for void space, and "1" labels for chalk solid matrix.

pressure– (MICP) measured pore size distribution. The MICP experiment is sensitive to the cross section of rock pores that limit the directional propagation of its front—the pore throat radii. Therefore, in interpreting the MICP measurements we assume cylindrical pore geometry [27,28].

Magnetic susceptibility values were obtained through experimental measurements using a magnetic susceptibility balance. The mean measured value of volumetric susceptibility was $\chi_{v,c} = 16 \times 10^{-6}$ for chalk and $\chi_{v,w} = -8.9 \times 10^{-6}$ for water in SI units. The corresponding internal field map was calculated using the magnetic dipole approximation [29]. The 380^3 sample subset was chosen to avoid wrap-around errors in the calculated internal field near the external domain boundary.

Magnetization decay data was obtained using the previously described simulated CPMG procedure, utilizing Algorithm 1 to compute the time evolution of the system state; this was carried out for two echo times, $t_E = 100$ μs and $t_E = 1000$ μs. Computations utilized 1440 Intel Xeon Platinum 8274 processors @3.2 GHz on an InfiniBand cluster. The resulting transverse magnetization data were subjected to a numerical inverse Laplace transform to recover its T_2 relaxation time spectrum [30,31].

Other simulation specifications, such as field strength, are set to values used in experimental NMR measurements for a direct comparison of the results. The NMR experiments were carried out at two field strengths using a Magritek Rock Core Analyzer (operating at proton resonant frequency of 2 MHz) and a benchtop Magritek Spinsolve Carbon spectrometer (43 MHz for ^{1}H). The chalk core specimen was saturated with a water-based brine containing 7% by weight $MgCl_2$, $CaCl_2$, and NaCl following Ref. [32], which demonstrated that this fluid composition maintains matrix structural integrity and prevents weakening for at least 6 weeks, which fully covered the time spans of the NMR acquisitions. The main coil of the NMR device produces a field of 0.047 T, corresponding to 2-MHz frequency for ^{1}H.

The CPMG pulse-echo experiment is carried out on chalk for echo times of $t_E = 100$ μs and $t_E = 1000$ μs at 2 and 43 MHz. These experimental data are compared to NMR-LBM outputs under simulation settings mimicking experiment. Acknowledging the variation in magnetic susceptibility between low and high magnetizing fields in carbonate rocks (owing to incomplete magnetization of the ferromagnetic inclusions of the solid matrix under a weak field), the input susceptibility $\chi_{v,c}$ is increased at 43 MHz to account for the nonlinear field-magnetization relationship [33,34].

The comparison criteria constituted monoexponential least-squares decay constant fitting and weighted logarithmic mean of the Laplace-inverted spectra, as well as the spectra themselves. These results are presented in Tables I and II and Figs. 7 and 8. A negative shift in modal peak placement at the longer echo time is observed in all instances; at 2 MHz, both experimental and simulated data agree in the direction of the shift, though the effect is strongest in the experimental spectra. Peak broadening is observed—both experimental and simulated spectra exhibit a wider peak at the longer echo time, though the experimental spectra demonstrate a stronger sensitivity than simulations. At 43 MHz, between $t_E = 100$ μs and $t_E = 1000$ μs, good agreement is observed in modal

TABLE I. Monoexponential T_2 relaxation time fit and logarithmic mean comparison of inverted spectra for simulation and experiment (2 MHz)

	Monoexp. fit (ms)			Log-mean (ms)		
t_E	EXP	SIM	RW	EXP	SIM	RW
100 μs	25.74	26.30	22.50	24.29	25.56	21.17
1000 μs	24.18	26.20	22.44	22.76	25.36	21.06

relaxation times and the relative shift between echo intervals is comparable.

At 2 MHz, the modal relaxation time of ∼22 ms reported by the RW method for chalk is shorter than the modes obtained by experiment or NMR-LBM, which both report ∼26 ms. The relaxation time responses to the echo spacing are mutually coherent with the NMR-LBM results, with a negative relaxation time shift and a peak broadening accompanying an increase in echo time. We note that the difference between numerical solvers is well within the variation range of A describing the specifics of implicit surface area treatment.

In addition to magnetization responses integrated over the 380^3 system in CPMG numerical experiments, fully resolved tomogram-scale magnetization density maps reported by NMR-LBM for the chalk system are presented. These constitute functional field (transverse magnetization density, m_y) evolution snapshots during a simulated CPMG pulse-acquisition sequence at a set of time points, wich linear multiples of echo time t_E chosen so that the prevailing relaxation modes are visually discernible. Two-dimensional xy cross sections of these maps at 4, 159, and 318 echo time intervals $t_E = 100$ μs, corresponding to $t = 0.4$, 15.9, and 31.8 ms (1260 δt, 50076 δt, and 100156 δt correspondingly in discrete time; $\delta t = 3.175 \times 10^{-4}$ ms), are shown in Fig. 9. Magnetization density contours are clearly observed and curve inwards from the solid boundary in accord with pore geometry, becoming spherical in large spherical pores. Larger pores exhibit higher net nonequilibrium magnetization. Interpore magnetization exchange is apparent as there are smooth transient gradients between pores of contrasting sizes and an associated directional change of magnetization curvature.

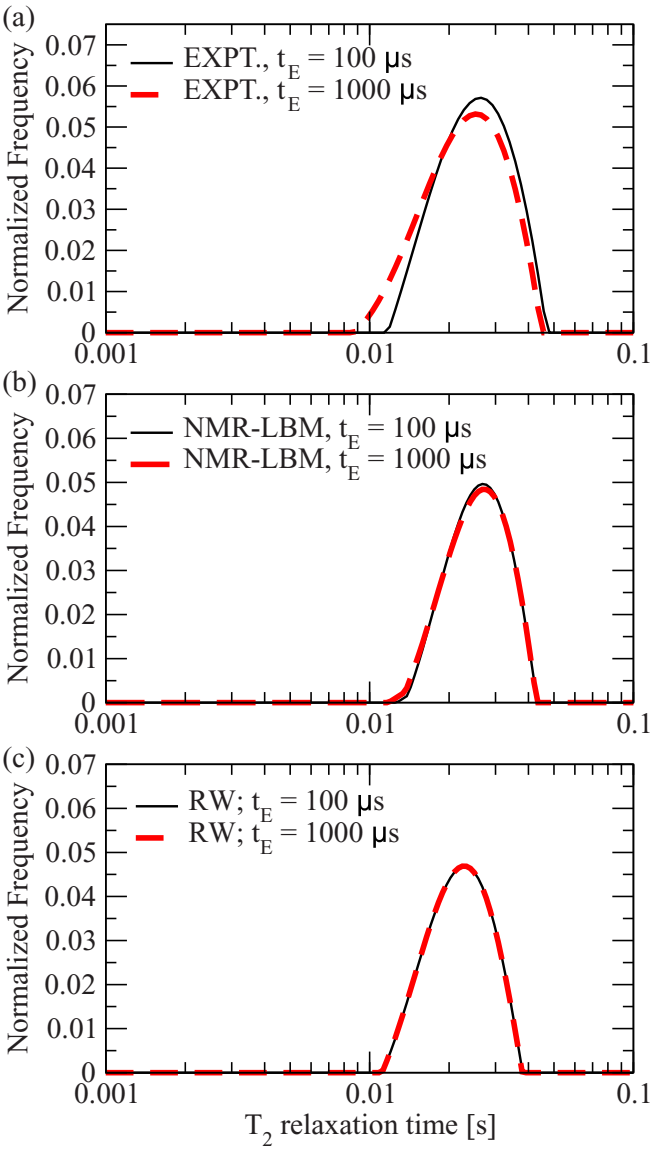

FIG. 7. Spectral profiles of (a) experimental acquisitions and (b) NMR-LBM simulations and (c) random-walk simulations on chalk at 2 MHz; $t_E = 100$ μs and $t_E = 1000$ μs.

VI. DISCUSSION

The comparison of experiment and simulations for the chalk sample showed good agreement in transverse relaxation time modes but had discrepancies in the width of the distribution between experiment and simulation, as well as differences in the relative peak placement for the numerical solvers. These observations are discussed systematically: First, the intersolver discrepancies are addressed, followed by evaluating the chalk sample using simulated NMR-LBM data.

TABLE II. Monoexponential T_2 relaxation time fit and logarithmic mean comparison of inverted spectra for simulation and experiment (43 MHz).

	Monoexp. fit (ms)		Log-mean (ms)	
t_E	EXP	SIM	EXP	SIM
100 μs	15.68	15.18	14.69	14.55
1000 μs	7.09	6.97	6.92	6.63

A. Solver surface treatment

To justify shorter T_2 modes reported by random-walk simulations for chalk, we consider Fig. 5; the relative difference between the solvers is small in low-resolution sphere discretizations and increases asymptotically to a constant factor in the limit of resolution. The modal discrepancy is attributed to a fundamental difference in the incorporation of surface relaxation between given solver paradigms, as a result of which the two solvers differ in the probed surface area. The six-neighborhood random-walk code sees the surface area at any solid-adjacent fluid site as a discrete collection of

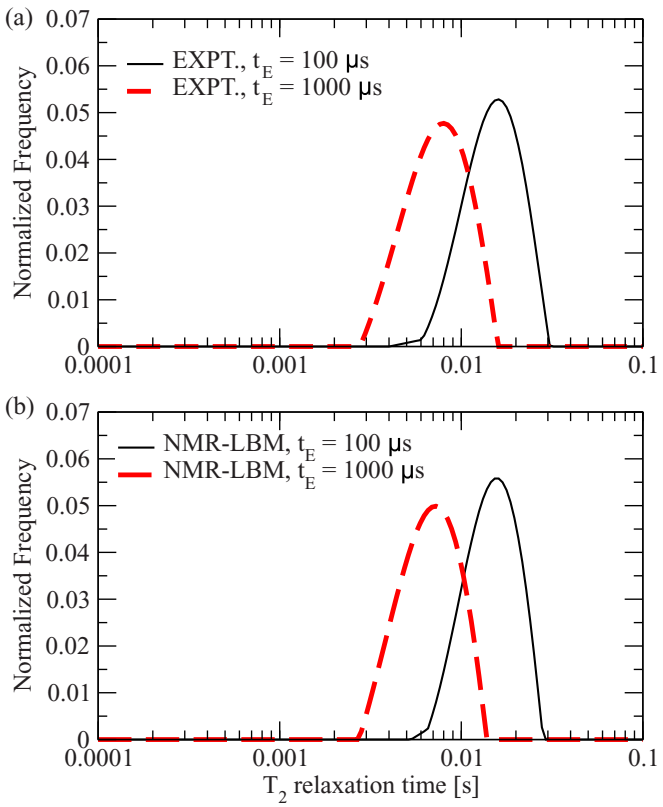

FIG. 8. Spectral profiles of (a) experimental acquisitions and (b) NMR-LBM simulations on chalk at 43 MHz; $t_E = 100\ \mu$s and $t_E = 1000\ \mu$s.

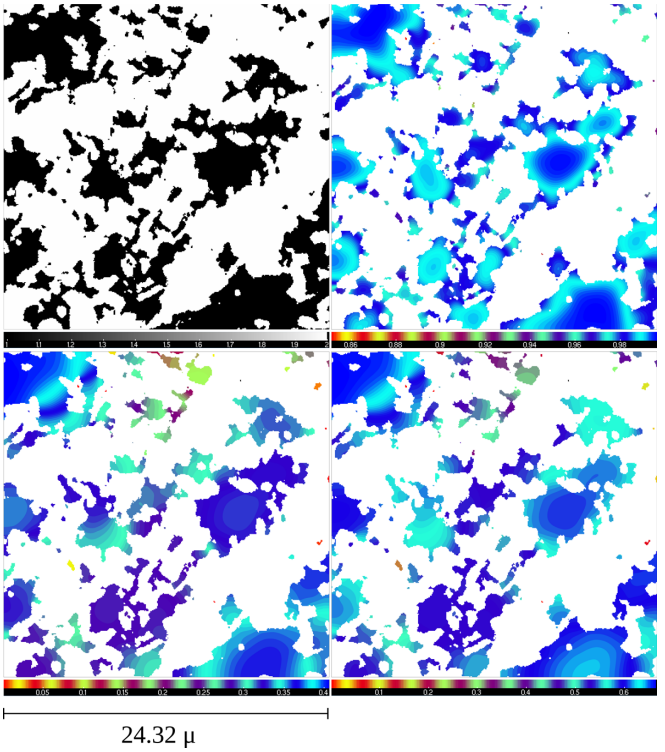

FIG. 9. Clockwise from top right: Two-dimensional xy plane slices through the 380^3 transverse magnetization density map taken during along a CPMG sequence at 4, 159, and 318 echoes at $t_E = 100\ \mu$s; 2D xy slice through the chalk tomogram at the same z coordinate. Chalk solid matrix is illustrated in white and void is in black.

orthogonal boundary voxel areas. Conversely, in NMR-LBM surface relaxation in any such fluid voxel is a superposition of attenuations induced by each lattice stream directed to, and reflected from, the neighboring solid matrix sites, including corners between them: Up to 26 simultaneous contributions to magnetization attenuation are thus theoretically possible (Fig. 1). Due to its incorporation of lattice weights, streams reflected from more distant boundary contacts within the Cartesian lattice ($||\mathbf{e}_i|| = \sqrt{2}$, "diagonal" or $||\mathbf{e}_i|| = \sqrt{3}$, "double-diagonal") inherently effect a weaker relaxation at the parent voxel. This is due to the distance-based weights derived for a discrete lattice superimposed on a continuum spherically symmetrical probability distribution function in free space. Therefore, NMR-LBM probes the lattice area as a discretization of a spatially continuous field, while RW treats it as being strictly discrete and corrects for over-relaxation at the corners with a constant correction factor. Considering that the specific correction factor for chalk is not known, that RW returns a faster decay in spherical pores (Fig. 5), and that the chalk simulation domain is not strongly aspherical (Fig. 9), the observation of a shorter modal transverse relaxation time in RW simulations as compared to NMR-LBM is consistent.

B. Structural heterogeneity

Consider first that the chalk sample in the simulation is a cubic phase field of side length 24.32 μm, corresponding to 380^3 nano-CT voxels. This resolution is required to calculate the NMR response at the resolved pore scale. The sample visually captures the characteristic microstructure and a representative elementary volume (REV) is assumed, where this REV represents matrix porosity. We tested this assumption by acquiring a micro-CT image with voxel size of 688 nm, a cross section of subsection of which is depicted in Fig. 10. The simulation domain based on the nano-CT image of the matrix porosity region corresponds to about 35^3 micro-CT voxels. Larger pores or grains with microporosity may give rise to a broader distribution of relaxation times as observed experimentally and can be observed visually from the micro-CT images. Note that the MICP-based pore size distribution would not be affected by the occurrence of these larger pores as they are not themselves forming a percolating network. Furthermore, the larger heterogeneity in material distributions and a small fraction of larger pores would give rise to an increase in dephasing for larger echo times which is not sampled in the numerical simulations due to the simulation domain not incorporating any of the larger pores. Furthermore, mineral inclusions which are not seen in the simulation domain but exist in the experimental sample generate gradients across smaller pores which contribute to faster coherence loss in the pore network fraction in the vicinity of such mineral inclusions.

C. Signal processing

A second possible source of mismatch between experimental measurement and numerical simulation of T_2 distributions

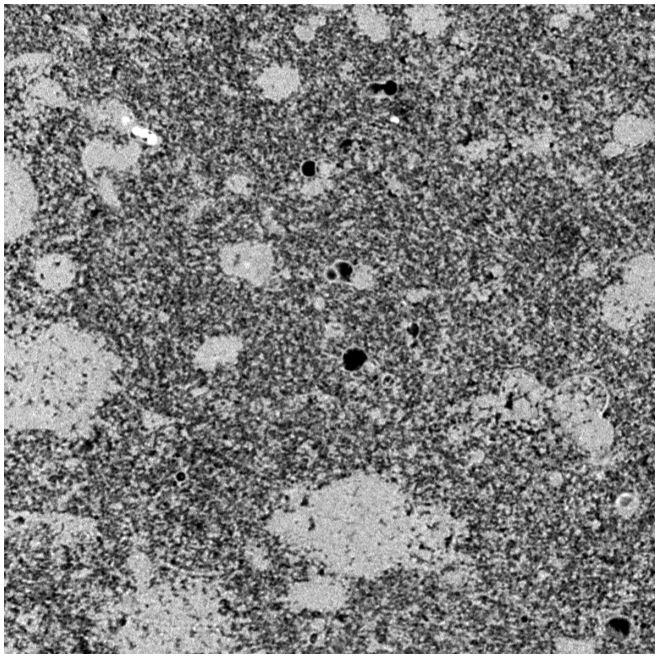

FIG. 10. Cross section through a subsection of a micro-CT tomogram of the chalk sample at a resolution of $\epsilon = 688$ nm with a field of view of 1200^2 voxels, illustrating both the predominant matrix porosity, and larger-scale "vugs" as well as larger-scale solid grains.

is the absence of experimental noise in the simulated data. Experimental noise is mimicked by distorting simulated $S_{xy}(t)$ decay data with white Gaussian noise ($\mu = 0$, SNR $= 300$) incorporating a signal-to-noise ratio of 300 and a mean offset of 0 prior to inversion. Acknowledging the sensitivity of multiexponential approximations of ill-conditioned criteria to the choice of regularization specifics, the same Tikhonov-stabilized inversion algorithm was utilized for all inversions; the T_2 inversion axis contains 200 logarithmically spaced points between 5 μs and 1 s. The inverted spectra are subjected to normalization, which limits useful comparison criteria to the placement of spectral maxima in the frequency domain and the general spectral shape, as measured by a weighted logarithmic mean over the chosen Laplace subdomain.

D. Idealizing assumptions

An additional source of mismatch for the magnitude of the echo time effect between experiment and simulations are the physical assumptions implicitly made in both NMR-LBM and RW simulation algorithms. While any simulated experiment could not account for all aspects of the experimental physics, we highlight (1) imperfections in the applied magnetic field pulses and (2) heterogeneities in the field produced by the main coil of the NMR tool as the dominant experimental imperfections not incorporated in the simulations.

The echo time effect observed in the simulated data, though weak, exhibits a relaxation time trend consistent with NMR theory—specifically, that sparser echo spacing results in less efficient refocusing of dephasing spins under self-diffusion over a time interval and resulting in a faster coherence loss [23,35,36]. The random-walk results from simulations on the same chalk system, utilizing the same idealizing assumption of hard RF pulses, likewise exhibited a weak relaxation time shift in comparison to experiment. Ignoring the above sources of experimental error, this suggests that the magnetization evolution in the chalk system is dominated by surface interactions; the magnetic heterogeneity of the environment has a much smaller contribution to magnetization loss. Qualitatively, magnetization density maps in Fig. 9 exhibit curvature shaped primarily by the morphology of the constraining solid matrix, exhibiting the steepest magnetization gradients along directions normal to the pore walls, suggesting surface relaxation as the dominant driver of magnetization evolution in chalk.

Concerning the comparison at 43-MHz frequency, though the absolute placement of spectral modes differs between simulation and experiment, their relative shift as a function of echo spacing is close to a factor of 2 in both simulated and experimental data. Note the fact that the T_2 surface relaxivity for chalk is left unchanged when switching to a higher flux density. Acknowledging that a stronger external field would result in an increased surface relaxivity parameter for T_2, the longer relaxation times reported by the simulation in absence of any relaxivity adjustment are consistent.

VII. CONCLUSION

An NMR simulation framework utilizing the lattice Boltzmann method to resolve the macroscopic Bloch-Torrey equations has been implemented and validated. The incorporation of tomogram-scale magnetization exchange with 26 neighbors avoids the limitations of models with diffusionally closed computational voxels, enabling NMR simulations on complex media at fine resolution. Excellent agreement between simulations and analytical solutions is demonstrated. At low field strength of 2 MHz, the numerical approach accurately reproduces experimentally observed spectral peak modes at short echo times. The experimentally observed effects of echo time variation are reproduced to a lesser extent due to idealizing physical assumptions of the model system and experimental procedures. Results provided by similarly ideal random-walk simulations display a similar order of these effects. At higher field of 43 MHz, good agreement is observed between simulated T_2 relaxation time measures and those derived from experimental acquisitions. Magnetization evolution modes of the chalk sample exhibit a strong sensitivity to the morphology of the pore structure, and a small contribution from the internal field inhomogeneities is observed through minor shifts in relaxation time by varied echo spacing. The latter is corroborated through visual inspection of magnetization ground mode curvature on images of the whole system's magnetization density facilitated by NMR-LBM. The method's computational implementation allows straightforward extension to arbitrary NMR pulse and acquisition configurations. Parallel implementation enables analysis of large sample domains on HPC clusters. In future work we plan to utilize the LBM framework for the analysis of diffusion-relaxation eigenmodes of complex systems and include the analysis of NMR responses under flow conditions.

ACKNOWLEDGMENTS

C.H.A. thanks the Australian Research Council (ARC) for funding through discovery Grant No. DP190103744. This research was undertaken with the assistance of resources and services from the National Computational Infrastructure (NCI), which is supported by the Australian Government. We acknowledge Matthew Andrew of Zeiss for kindly acquiring nano-XCT images of the chalk sample and Ji-Youn Arns for respective image processing.

[1] P. Basser, J. Mattiello, and D. LeBihan, Biophys. J. **66**, 259 (1994).

[2] A. Wieland, D. de Beer, L. R. Damgaard, M. Kühl, D. van Dusschoten, and H. V. As, Limnol. Oceanogr. **46**, 248 (2001).

[3] B. Kresse, M. Hofmann, A. F. Privalov, N. Fatkullin, F. Fujara, and E. A. Rössler, Macromolecules **48**, 4491 (2015).

[4] A. Pohlmeier, S. Haber-Pohlmeier, and S. Stapf, Vadose Zone J. **8**, 735 (2009).

[5] R. J. S. Brown and I. Fatt, Petrol. Trans. (AIME) **207**, 262 (1956).

[6] B. Robertson, Phys. Rev. **151**, 273 (1966).

[7] C. Neuman, J. Chem. Phys. **60**, 4508 (1974).

[8] K. R. Brownstein and C. E. Tarr, Phys. Rev. A **19**, 2446 (1979).

[9] A. L. Sukstanskii and D. A. Yablonskiy, J. Magn. Reson. **157**, 92 (2002).

[10] T. S. Ramakrishnan, L. M. Schwartz, E. J. Fordham, W. E. Q. Kenyon, and D. J. Wilkinson, Log Anal. **40**, 260 (1999).

[11] E. Toumelin and C. Torres-Verdín, SPE Reservoir Eval. Eng. **6**, 234 (2003).

[12] C. H. Arns, T. AlGhamdi, and J.-Y. Arns, New J. Phys. **13**, 015004 (2010).

[13] P. R. Connolly, W. Yan, D. Zhang, M. Mahmoud, M. Verrall, M. Lebedev, S. Iglauer, P. J. Metaxas, E. F. May, and M. L. Johns, J. Pet. Sci. Eng. **175**, 985 (2019).

[14] H. C. Torrey, Phys. Rev. **104**, 563 (1956).

[15] D. Bytchenkoff and S. Rodts, J. Magn. Reson. **208**, 4 (2011).

[16] T. H. Jochimsen, A. Schäfer, R. Bammer, and M. E. Moseley, J. Magn. Reson. **180**, 29 (2006).

[17] N. M. Naughton, C. G. Tennyson, and J. G. Georgiadis, Phys. Rev. E **102**, 043305 (2020).

[18] A. Sakellariou, C. H. Arns, A. P. Sheppard, R. M. Sok, H. Averdunk, A. Limaye, A. C. Jones, T. J. Senden, and M. A. Knackstedt, Mater. Today **10**, 44 (2007).

[19] S. Chen and G. D. Doolen, Annu. Rev. Fluid Mech. **30**, 329 (1998).

[20] H. Chen, S. Chen, and W. H. Matthaeus, Phys. Rev. A **45**, R5339(R) (1992).

[21] K. Suga, Y. Kuwata, K. Takashima, and R. Chikasue, Comput. Math. Appl. **69**, 518 (2015).

[22] A. Hiorth, U. H. a Lad, S. Evje, and S. M. Skjæveland, Int. J. Numer. Methods Fluids **59**, 405 (2009).

[23] H. Y. Carr and E. M. Purcell, Phys. Rev. **94**, 630 (1954).

[24] S. Meiboom and D. Gill, Rev. Sci. Instrum. **29**, 688 (1958).

[25] A. P. Sheppard, R. M. Sok, and H. Averdunk, Physica A **339**, 145 (2004).

[26] D. Wildenschild and A. P. Sheppard, Adv. Water Resour. **51**, 217 (2013).

[27] Z. Cao, G. Liu, C. Li, Y. You, C. Yang, and H. Jiang, Sci. Rep. **6**, 36919 (2016).

[28] Y. Yuan and R. Rezaee, Energies **12**, 2094 (2019).

[29] Y.-Q. Song, Concepts Magn. Reson. **18A**, 97 (2003).

[30] C. L. Lawson and R. J. Hansen, *Solving Least Squares Problems* (Prentice-Hall, Hoboken, NJ, 1974)

[31] P. C. Hansen, Inverse Probl. **8**, 849 (1992).

[32] T. Heggheim, M. Madland, R. Risnes, and T. Austad, J. Pet. Sci. Eng. **46**, 171 (2005).

[33] D. K. Potter, T. M. AlGhamdi, and O. P. Ivakhnenko (Society of Core Analysts, Houston, TX, 2018).

[34] F. Hrouda, Geophys. J. Int. **150**, 715 (2002).

[35] J. M. Gomori, R. I. Grossman, C. Yu-Ip, and T. Asakura, J. Comput. Assist. Tomogr. **11**, 684 (1987).

[36] V. G. Kiselev and D. S. Novikov, NeuroImage **182**, 149 (2018).